Koivunen, Risto; Bollström, Roger; Gane, Patrick

Inkjet jettability and physical characterization of water-ethanol solutions of low molecular weight sodium polyacrylate and poly-diallyl dimethyl ammonium chloride (polyDADMAC)

Published in:
AIP Advances

DOI:
10.1063/5.0006634

Published: 01/05/2020

Document Version
Publisher's PDF, also known as Version of record

Please cite the original version:
Koivunen, R., Bollström, R., & Gane, P. (2020). Inkjet jettability and physical characterization of water-ethanol solutions of low molecular weight sodium polyacrylate and poly-diallyl dimethyl ammonium chloride (polyDADMAC). *AIP Advances*, *10*(5), Article 055309. https://doi.org/10.1063/5.0006634

AIP Advances

Inkjet jettability and physical characterization of water–ethanol solutions of low molecular weight sodium polyacrylate and poly-diallyl dimethyl ammonium chloride (polyDADMAC)

Cite as: AIP Advances **10**, 055309 (2020); https://doi.org/10.1063/5.0006634
Submitted: 04 March 2020 . Accepted: 23 April 2020 . Published Online: 08 May 2020

Risto Koivunen, Roger Bollström, and Patrick Gane

COLLECTIONS

Paper published as part of the special topic on Chemical Physics, Energy, Fluids and Plasmas, Materials Science and Mathematical Physics

AIP Advances ARTICLE scitation.org/journal/adv

Inkjet jettability and physical characterization of water–ethanol solutions of low molecular weight sodium polyacrylate and poly-diallyl dimethyl ammonium chloride (polyDADMAC)

Cite as: AIP Advances 10, 055309 (2020); doi: 10.1063/5.0006634
Submitted: 4 March 2020 • Accepted: 23 April 2020 •
Published Online: 8 May 2020

Risto Koivunen,[1,a)] Roger Bollström,[1,2] and Patrick Gane[1]

AFFILIATIONS

[1] Department of Bioproducts and Biosystems, School of Chemical Engineering, Aalto University, P.O. Box 16300, FI-00076 Aalto, Finland

[2] Omya International AG, Baslerstrasse 42, CH-4665 Oftringen, Switzerland

[a)] **Author to whom correspondence should be addressed:** risto.koivunen@aalto.fi. **Tel.:** +358 50 4061259

ABSTRACT

Polyelectrolytes are water-soluble polymers having repeat units carrying electrolyte groups. As polyionic molecules having like charge units, they are self-repelling with a rod-like conformation in solution. Inkjet applications of polyelectrolytes include particle dispersing, surface modification, and multilayer structures. This work investigates the physical properties of low molecular weight sodium polyacrylate (NaPA) and poly-diallyl dimethyl ammonium chloride (polyDADMAC) polyelectrolyte solutions in the water–ethanol mixture in relation to their behavior in inkjet deposition. In rotational rheometry measurements, the solutions are found to behave in a Newtonian fashion once the effects of experimental artifacts are taken into account. The range of NaPA concentrations that could be studied was limited to 1 wt./wt. % by the poor solubility of NaPA in the presence of ethanol, and at these concentrations, the addition of NaPA to the solvent did not have a significant effect on the jetting behavior. PolyDADMAC had good solubility, and concentrations up to 10 wt./wt. % were studied and jetted successfully. While an increase in polyelectrolyte concentration resulted in a slow increase in ink viscosity, this was not found to have a significant effect on the required jetting voltage or maximum stable jetting frequency, though drop detachment and satellite droplet formation times were found to increase. As a practical limitation of polyDADMAC inks, solvent evaporation was found to lead to idle nozzles becoming non-jetting, with the allowed idle time decreasing rapidly as ink polyDADMAC concentration increased. This non-jetting behavior is likely due to residence time at the nozzle exit leading to the local surface tension and/or viscosity increase, differing from the bulk ink properties.

INTRODUCTION AND BACKGROUND

Polyelectrolytes are water-soluble polymers that display electrical charge when dissolved, typically due to dissociation of ionic bonds. Polyelectrolytes are, therefore, self-repelling by nature, with charged segments of the polymer chain acting via their electrical potential to maintain separation from each other. This electrostatic repulsion in aqueous solution results in the polymer molecule adopting a rod-like minimum energy conformation, in contrast to the more coiled conformation of neutral polymers. A common industrial application of this charged nature is as an electrostatic dispersing agent, with the surface-adsorbed polyelectrolyte causing microscale or nanoscale particles to repel each other, thus preventing agglomeration.

In the field of inkjet ink development, polyelectrolytes can be studied either as dispersing agents in particulate inks, such as copper nanoparticles for printed electronics (Tam *et al.*, 2016) and thermoplasmonic gold nanoparticles for security printing

(Kang *et al.*, 2018), or as pure polymer solutions. Inkjet deposited polyelectrolyte solutions have been employed, for example, to pattern glass surfaces to attract oppositely charged nanoparticles (Leigh *et al.*, 2015) and in the fabrication of multi-layer structures for pH sensors (Jovic *et al.*, 2018). Alternatingly, deposited layers of anionic and cationic polyelectrolyte solutions have been employed to build permeable hydrogels (Limem and Calvert, 2015), thin films, or, when combined with a sacrificial template, even nanotubes (Gao *et al.*, 2016).

The present authors have previously studied various inkjet deposited polyelectrolyte solutions for locally adjusting surface chemistry and chromatographic properties of porous pigment coatings intended as analytical platform elements (Koivunen *et al.*, 2017; 2019). Like many published studies with inkjet deposited polyelectrolytes, these earlier studies were conducted with just a single concentration level, 1 wt./wt. %. The amount of the deposited polyelectrolyte was instead adjusted by printing multiple ink layers, with a drying stage in between—a convenient approach for research purposes but impractical for production, where a desired quantity is preferably deposited in a single printing step.

In the present work, the authors complement their previous investigations by studying the effect of increasing polyelectrolyte concentration both on the physical properties and on the jetting behavior of low M_w sodium polyacrylate (NaPA) and poly-diallyl dimethyl ammonium chloride (polyDADMAC) water–ethanol solutions. Commonly studied physical properties of inkjet inks, regardless of their composition, include density, surface tension, and viscosity. Out of these, density and surface tension are slightly temperature-dependent but are otherwise unaffected by environmental conditions encountered inside the printhead. Viscosity, however, is not only highly temperature-dependent but possibly also dependent on the measuring environment, as the behavior of non-Newtonian fluids can be affected by both the shear rate and the time-scale (frequency) of the flow; within the inkjet, printhead ink is typically exposed to high shear rates over a short time period.

Underlying the rheological response of polyelectrolyte ink in the inkjet process is its dependence on both polymer concentration and molecular weight (M_w). Inkjet deposition studies conducted with varying concentrations and M_w of polystyrene dissolved in acetophenone (de Gans *et al.*, 2004) and diethyl phthalate (Hoath *et al.*, 2012), for example, have demonstrated that the maximum jettable polymer concentration can reduce drastically as polymer M_w increases, in a way that cannot always be directly related to shear viscosity.

Rotational rheometry, where the resistance of a thin layer of the liquid to shearing between a static and a rotating surface is measured, is a common method for determining viscosity under a controlled range of shear rates and oscillation frequencies. However, it is potentially affected by numerous experimental artifacts, which can be broadly classified as hardware- or sample-related (Stadler, 2014). Hardware-related artifacts include mechanical imperfections or misalignment in measuring geometries, thermal gradients, and expansion of measuring geometries, hardware inertia, and centrifugal effects (Stadler, 2014). Sample-related artifacts include bubbles (Wolff and Münstedt, 2013), dissipative heating (Laun *et al.*, 2014), overfilling (Cardinaels *et al.*, 2019), phase separation and wall slip (Marquardt and Nijman, 1993), and solvent evaporation during measurement and material degradation due to temperature or shear conditions (Stadler, 2014). The presence of artifacts can be investigated with Newtonian model fluids to determine reliable measurement settings for a particular instrument, geometry, and sample type (Laun *et al.*, 2014; Zhang *et al.*, 2018).

Low viscosity fluids, such as inkjet inks, are particularly prone to artifacts in rotational rheometry, which may result in apparent non-Newtonian behavior of actual Newtonian samples. For example, at low shear rates, measurements can be affected by the torque resolution sensitivity of the hardware (Marquardt and Nijman, 1993), or by random contact line asymmetries causing non-deterministic apparent shear thinning (Johnston and Ewoldt, 2013). At high shear rates, the centrifugal effect causes geometry-dependent secondary flows, resulting in apparent shear thickening of the sample. In concentric circle geometries, Taylor vortices manifest when a critical rotational velocity is exceeded (Taylor, 1923), while in cone and plate geometries, tangential secondary flows manifest themselves gradually with increasing rotational velocity (Turian, 1972). With high frequency oscillation, further artifacts can be caused by sample and instrument inertia as measurement frequency increases, and by errors in phase angle determination due to noisy data (Velankar and Giles, 2007; Laun *et al.*, 2014).

Piezoelectric drop-on-demand inkjet technology operates by applying an electrical signal of specific voltage into a piezoelectric element, mounted within the printhead pump chamber, which expands by a controlled volume and forces the surrounding ink into motion, pushing an ink column toward the nozzle exit and forming a droplet out of the nozzle exit. Inertial and surface tension effects cause this column to detach from the nozzle, forming one or more droplets. The pressure imparted by the piezoelectric element is transferred into kinetic energy of the ink column, as well as becoming partially dissipated as heat due to viscous damping. Part of this kinetic energy is consumed to overcome surface tension to form a new drop, while the rest remains either as kinetic energy of the newly formed drop or as oscillating mechanical energy of the ink within the printhead. Thus, the bulk liquid inside the printhead does not come to rest immediately after drop expulsion, but, instead, the remaining mechanical pressure wave can affect the following, and subsequent, jetting cycle(s) until damped out.

The aim of this experimental work is to investigate the effect of increasing polyelectrolyte concentration and resulting physical ink characteristics on (i) jetting parameters of actuation voltage and frequency, (ii) drop formation in terms of drop detachment and satellite droplet formation, and (iii) practical limitations of jettable formulations. Particular attention is paid to possible rheometrical artifacts in the physical characterization.

MATERIALS AND METHODS

Materials

Studied polyelectrolytes were 8.5 kDa M_w cationic polyDADMAC (Polysciences, Inc., Warrington, USA, product code 24828-100), supplied as an aqueous solution with 28 wt./wt. % nominal and 27.4 ± 0.4 wt./wt. % measured solid content, and 8 kDa M_w anionic sodium polyacrylate (Sigma-Aldrich, St. Louis, USA, product code 416029), also supplied as an aqueous solution with 45 wt./wt. % nominal and 41.0 ± 0.3 wt./wt. % measured solid content.

The prepared series of polyelectrolyte solution concentrations consisted of 0.1 wt./wt. %, 0.2 wt./wt. %, 0.5 wt./wt. %, 1.0 wt./wt. %, 2.0 wt./wt. %, 3.0 wt./wt. %, 4.0 wt./wt. %, 5.0 wt./wt. %, 7.5 wt./wt. %, and 10.0 wt./wt. % polyelectrolyte, respectively, 25 wt./wt. % ethanol, and de-ionized water (rest). Additional water–ethanol reference solution consisted of 25 wt./wt. % ethanol and 75 wt./wt. % de-ionized water.

Newtonian reference samples for rheometrical experiments consisted of 0 wt./wt. %, 30 wt./wt. %, 50 wt./wt. %, 60 wt./wt. %, 70 wt./wt. %, and 75 wt./wt. % glycerol (ICN Biomedicals, United States, or Merck KGaA, Darmstadt, Germany), respectively, in de-ionized water.

Rotational rheometry

Rotational measurements were conducted with an MCR 302 rheometer (Anton Paar, Graz, Austria) with a DG 26.7 double gap geometry, in which a hollow cylindrical bob rotates coaxially in the annular gap between the walls of a narrow double-walled cylindrical cup, mounted on a Peltier-controlled C-PTD200 cup-holder, set at 30 °C and covered with a CV-CYL/Q disc to limit evaporation. Such a geometry provides a symmetrically oriented shear field about the cylinder element, as well as a large contact area between the sample fluid and the cylinder surfaces.

Before measurement, 5 cm^3 of the sample was pipetted into the double-walled gap while the cup was held at an angle, and afterward, the cup was visually inspected with the help of a flashlight to ensure that no large air bubbles were present in the gap. The measurement cup was then mounted on the cup holder, and the hollow measuring bob was lowered by its attached spindle into position. Excess sample (~1.2 cm^3) was removed with a flexible pipette through holes on top of the bob. Subsequently, the cup was covered with the lid and the whole setup was allowed to equilibrate to the measurement temperature.

The measurement cycle employed consisted of a series of steady shear and frequency sweep segments, listed in Table I. These were intended to measure steady shear viscosity at low (No. 5) and high (No. 10) shear rates, as well as oscillational behavior at varying frequencies (No. 8), with the rest of the segments intended as pre-shearing steps. Three parallel samples were measured at each concentration level.

Other fluid characterization methods

Solution density was measured by removing 4 cm^3 of the sample with a pipette from a sample in a container and measuring the resulting difference in the sample and container weight before and after the sample removal, with the procedure being repeated 10 times per sample. Surface tension was measured with a CAM200 instrument (KSV Instruments, Helsinki, Finland) at 21 °C from nominally 2–4 μl pendant drops formed by an integral dispenser, with five drops tested per sample, each measured ten times at 1 s intervals.

Ink jetting characterization

Ink jetting was studied with a DMP-2831 inkjet printer (Fujifilm Dimatix, Santa Clara, USA) employing a drop-on-demand printhead and integral drop watcher camera. Before use in jetting experiments, inks were filtered through 0.45 μm GHP Acrodisc GF syringe filters (Pall Corporation, Port Washington, USA), loaded in DMC-11610 cartridges with ~21.5 × 21.5 mm^2 rectangular nozzles, and allowed to rest for at least 40 h to permit possible air bubbles introduced during filtering to escape.

All jetting experiments were performed with the custom waveform described in Table II, with parameters experimentally chosen to provide acceptable jetting with the water–ethanol solvent mix alone, and then applied unaltered to the polyelectrolyte-containing test inks. The cartridge temperature was set at 30 °C for all inks and meniscus vacuum backpressure at 4.0 in. H_2O (~10 mbar). Jetting experiments were conducted and recorded with the water–ethanol mixture and polyelectrolyte solutions of 0.5 wt./wt. %, 1.0 wt./wt. %, 2.0 wt./wt. %, 3.0 wt./wt. %, 5.0 wt./wt. %, 7.5 wt./wt. %, and 10.0 wt./wt. % concentrations, respectively.

The integral drop watcher camera on the printer was not capable of imaging individual drops, which employs instead a stroboscopic principle to form a composite image of deposited drops. The strobe delay can be adjusted in 1 μs increments, while the imaging system spatial resolution was ~2.6 μm per pixel. Due to setup

TABLE I. Rheometry measurement segments in the order employed. In segment No. 8, rheometer software determined the time length per measurement point, and angular momentum compensation was applied.

Rheometry segment no.	Type	Settings	Measuring points	Time per point(s)
1	Steady shear	1–3000 s^{-1} (logarithmic steps)	60	1
2	Steady shear	3000 s^{-1} (constant)	10	1
3	Steady shear	3000–1 s^{-1} (reverse logarithmic steps)	60	1
4	Steady shear	1 s^{-1} (constant)	20	1
5	Steady shear	1–20 s^{-1} (linear steps)	20	10
6	No shear	...	1	10
7	Frequency sweep	50 rad s^{-1} (constant), 100% strain	1	10
8	Frequency sweep	50–1 rad s^{-1} (linear steps), 100% strain	50	Auto
9	Steady shear	50 s^{-1} (constant)	1	10
10	Steady shear	50–9000 s^{-1} (linear steps)	180	3

TABLE II. Custom waveform for jetting experiments. Level indicates the relative voltage applied to the piezoelectric element during the waveform segment, and slew rate indicates the relative rate of voltage change between subsequent segments. Nominal transition time within the jetting segments from 0% to 100% level is ~2.4 μs.

Waveform segment	Level (%)	Slew rate	Duration (μs)
Jetting 1	100	0.40	7.040
Jetting 2	0	0.40	5.888
Non-jetting 1	20	0.40	7.040
Non-jetting 2	0	0.40	5.888

limitations, the jetting drop can be imaged with sharp focus up to 300–400 μm distance from the nozzle, depending on the individual cartridge, and then with poorer focus between 700 and 1200 μm from the nozzle, with an obscured (dark image) region in between. An example of a drop watcher image is shown in Fig. 1.

Drop formation was observed both at a constant jetting frequency of 5 kHz and with variable frequency up to 16.6 kHz. For constant 5 kHz frequency, the actuation voltages of five parallel nozzles (with exceptions of two and three nozzles for 7.5 and 10 wt./wt. % polyDADMAC solutions, respectively) were set so that the head of the drop would travel ~300 μm distance in 60 μs time. The jetting behavior was observed to determine times for the drop tail filament detachment from the nozzle, tail filament merging with the main drop, and, if present, satellite droplet breaking off and merging with the main drop. For further analysis, images were recorded with 6 μs, 12 μs, 18 μs, 24 μs, 30 μs, 36 μs, 42 μs, 48 μs, 54 μs, 60 μs, and 200 μs strobe delays. With variable frequency tests, the strobe delay was set at 60 μs, jetting frequency increased in 0.1 kHz increments (smallest increment allowed in the control software), and images were recorded for analysis if a shift in drop behavior was observed.

Finally, the stability of a nozzle over an idle period was studied at 5 kHz frequency by turning off the observed nozzles for 5 s, 10 s, 15 s, 20 s, 30 s, 60 s, 180 s, 300 s, 600 s, and/or 900 s, after which they were again turned on and jetting behavior was observed. During this period, the ink at the nozzle was stimulated by a tickle pulse, defined by the non-jetting waveform segments described in Table II. However, since the cartridge has no capping mechanism, solvent evaporation at the nozzle may take place.

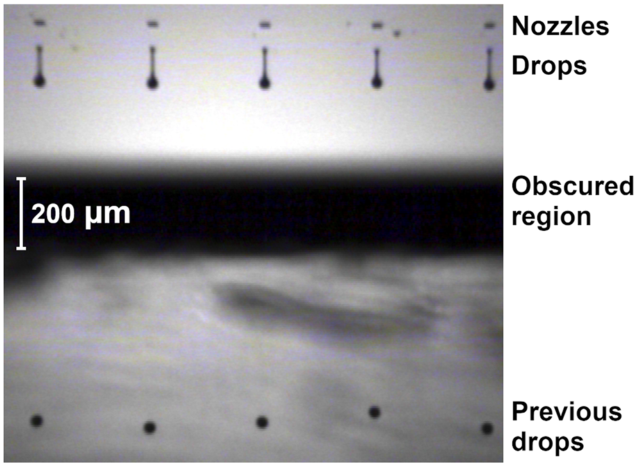

FIG. 1. Example of a drop watcher image on DMP-2831, showing five nozzles jetting 3 wt./wt. % polyDADMAC solution with a 30 μs strobe delay.

RESULTS AND DISCUSSION

Physical fluid properties

PolyDADMAC dissolved completely in the water/ethanol mixture at all of the tested concentrations. NaPA, with poor solubility in ethanol, dissolved uniformly in tested water–ethanol mixtures only up to 1 wt./wt. % concentration. At higher NaPA concentrations, two separate phases could be observed: a more viscous bottom layer, presumably consisting of NaPA and limited amount of water, and a less viscous top layer, presumably consisting of ethanol, water, and small amount of dissolved NaPA. Therefore, only NaPA solutions up to 1 wt./wt. % concentration in the water–ethanol mix were studied further.

The measured physical properties of polyelectrolyte solutions and reference glycerol mixtures are listed in Table III, together with calculated values for the inverse Ohnesorge number Oh^{-1} and the predicted and observed values for Taylor vortex manifestation. While polymer solutions can be potentially non-Newtonian fluids, due to the low M_w and self-repelling nature of the polyelectrolytes employed in this study, they are initially assumed to be Newtonian, and one viscosity value is given in Table III, respectively. However, this Newtonian fluid hypothesis is tested in the sections titled Steady shear viscosity measurements and Oscillational rheometry studies, with Taylor vortices discussed in the section titled Steady shear viscosity measurements.

The inverse Ohnesorge number Oh^{-1}, shown in Table III and encountered as a dimensionless parameter in numerous jetting studies, has been calculated as per the following equation:

$$Oh^{-1} = \frac{Re}{\sqrt{We}} = \frac{\sqrt{d\rho\sigma}}{\eta}, \tag{1}$$

where Oh stands for the Ohnesorge number, Re stands for the Reynolds number, We stands for the Weber number, ρ stands for the fluid density, η stands for the viscosity, σ stands for the surface tension, and d stands for the nozzle diameter (characteristic length). For the printhead in this work, the nozzle diameter is nominally 21.5 μm.

Ink viscosity expectedly increases with increasing polyelectrolyte concentration, though it remains relatively low even for the polyDADMAC 10.0 wt./wt. % preparation at 5.54 ± 0.04 mPa s, attributable to the low M_w of the polyelectrolyte product. For comparison, the manufacturer suggested maximum ink viscosity for the printhead is 30 mPa s and an ideal range 10–12 mPa s. The reference glycerol solutions were prepared and measured before the polyelectrolyte solutions, and therefore, they are needed to cover a wider range of possible viscosities so as to be sure of encompassing those of the polyelectrolyte solutions.

Ink densities are not significantly affected by the polyelectrolyte presence, ranging from 967 ± 4 kg m^{-3} for water–ethanol to 984 ± 3 kg m^{-3} for the polyDADMAC 10 wt./wt. % ink. Surface tension

TABLE III. Solution properties with 95% confidence intervals. Density and surface tension are measured at ∼20 °C. Viscosity is measured at 30 °C, reported as the average value measured at shear rates from 100 s^{-1} to 900 s^{-1}.

Sample	Density, ρ(kg m^{-3})	Surface tension, σ(mN m^{-1})	Viscosity, η (mPa s)	Oh^{-1}	Taylor vortex critical shear rate, $\dot{\gamma}_{\mathrm{crit}}$ (s^{-1})	
					Predicted	Observed
Glycerol 0 wt./wt. %	1002 ± 2	72.2 ± 0.2	0.82 ± 0.03	47.8 ± 1.3	892 ± 24	950
Glycerol 30 wt./wt. %	1076 ± 3	70.8 ± 0.3	1.91 ± 0.03	21.2 ± 0.3	1928 ± 24	1950
Glycerol 50 wt./wt. %	1130 ± 3	68.9 ± 0.5	4.33 ± 0.04	9.4 ± 0.1	4156 ± 39	4150
Glycerol 60 wt./wt. %	1154 ± 4	67.5 ± 0.3	6.96 ± 0.03	5.9 ± 0.1	6540 ± 30	6450
Glycerol 70 wt./wt. %	1180 ± 3	67.9 ± 0.4	14.42 ± 0.29	2.9 ± 0.1	13259 ± 266	NA
Glycerol 75 wt./wt. %	1195 ± 4	67.6 ± 0.4	21.24 ± 0.07	2.0 ± 0.1	19282 ± 88	NA
Water–ethanol (75:25 wt./wt. %)	967 ± 4	37.1 ± 0.6	1.71 ± 0.02	16.2 ± 0.3	1921 ± 23	1950
NaPA 0.1 wt./wt. %	971 ± 5	36.7 ± 0.5	1.77 ± 0.03	15.6 ± 0.3	1977 ± 34	2000
NaPA 0.2 wt./wt. %	974 ± 5	37.3 ± 0.7	1.80 ± 0.02	15.5 ± 0.3	2008 ± 23	2050
NaPA 0.5 wt./wt. %	979 ± 2	36.7 ± 0.6	1.88 ± 0.03	14.8 ± 0.3	2087 ± 27	2150
NaPA 1.0 wt./wt. %	982 ± 3	37.0 ± 0.7	1.96 ± 0.02	14.2 ± 0.2	2169 ± 23	2250
PolyDADMAC 0.1 wt./wt. %	970 ± 3	37.0 ± 0.5	1.79 ± 0.03	15.5 ± 0.3	2005 ± 26	2050
PolyDADMAC 0.2 wt./wt. %	972 ± 4	36.7 ± 0.6	1.85 ± 0.04	14.9 ± 0.3	2070 ± 38	2100
PolyDADMAC 0.5 wt./wt. %	969 ± 5	36.9 ± 0.7	1.95 ± 0.02	14.2 ± 0.2	2181 ± 23	2200
PolyDADMAC 1.0 wt./wt. %	970 ± 3	36.7 ± 0.5	2.11 ± 0.02	13.1 ± 0.2	2365 ± 24	2400
PolyDADMAC 2.0 wt./wt. %	973 ± 3	36.6 ± 0.5	2.39 ± 0.03	11.5 ± 0.2	2670 ± 24	2700
PolyDADMAC 3.0 wt./wt. %	970 ± 7	36.0 ± 0.6	2.72 ± 0.04	10.1 ± 0.2	3041 ± 46	3050
PolyDADMAC 4.0 wt./wt. %	972 ± 2	35.7 ± 0.6	3.06 ± 0.05	8.9 ± 0.2	3410 ± 51	3450
PolyDADMAC 5.0 wt./wt. %	975 ± 2	35.8 ± 0.5	3.39 ± 0.03	8.1 ± 0.1	3777 ± 31	3800
PolyDADMAC 7.5 wt./wt. %	980 ± 5	35.2 ± 0.6	4.34 ± 0.02	6.3 ± 0.1	4802 ± 29	4850
PolyDADMAC 10.0 wt./wt. %	984 ± 3	34.2 ± 0.8	5.54 ± 0.04	4.9 ± 0.1	6108 ± 44	6050

may seem to decrease as a function of increasing polyelectrolyte concentration, being ca. 37 mN m^{-1} for the low concentration and 34.2 ± 0.8 mN m^{-1} for the polyDADMAC 10 wt./wt. % ink. However, this is not likely due to the polyelectrolyte itself but rather due to the differing ratios of ethanol, 25 wt./wt. % for all inks, and water, ranging from 75 to 65 wt./wt. %, in the ink formulations.

Steady shear viscosity measurements

At low shear rates, Newtonian fluids in rotational rheometry may demonstrate apparent shear thinning due to non-deterministic contact line artifacts (Johnston and Ewoldt, 2013). In an effort to reduce the effect of these artifacts, the measurement cycle started with a shear ramp up from 1 to 3000 s^{-1} followed by a reverse ramp down (segment Nos. 1–3 in Table I). With reference glycerol samples, this was sufficient to remove contact line asymmetry in some of the samples, while in other cases, such artifacts still remained; examples of both are shown in Figs. 2(a) and 2(b), respectively. Therefore, the possibility of such artifacts needs to be considered when evaluating low shear rate viscosity measurements of low viscosity liquids.

The measured average viscosities for low shear rates, from 1 s^{-1} to 20 s^{-1}, corresponding to measuring segment No. 5, are shown in Fig. 3(a) and display a degree of apparent shear thinning between 1 s^{-1} and 5 s^{-1}. However, such effects may be simply due to contact line asymmetries; for comparison, Fig. 3(b) shows the flattest (Newtonian-like) viscosity curves out of the three parallel measurements. Comparing these results suggests that the apparent shear thinning observed in Fig. 3(a) is likely an artifact not reflecting the real material property, and the solutions are actually likely to behave in a Newtonian fashion over this shear rate range. As the contact line asymmetries are non-deterministic in nature, the confidence intervals in Fig. 3(a) can also be observed to increase as the shear rate decreases.

For inkjet applications, high shear rate behavior is of particular interest, since peak shear rates in printhead nozzles are typically estimated as being in the order of 10^5 s^{-1} (assuming, possibly questionably, laminar flow), recognized as lying well beyond the maximum of 9175 s^{-1} achievable with the rheometer test setup employed. As shown in Fig. 4, at shear rates from 50 s^{-1} to 9000 s^{-1}, corresponding to rheometry segment No. 10, the polyelectrolyte solutions demonstrate Newtonian behavior until Taylor vortices manifest. These secondary flows result in an additional torque response and respective apparent viscosity increase, setting a practical upper limit for the reliably measurable absolute viscosity range. Nonetheless, the emerging role of inertia, so important in the inkjet mechanism, becomes discernible.

In the case of Newtonian liquids, the critical shear rate at which the system manifests Taylor vortices in concentric circular or double gap rheometry depends on fluid properties and dimensions of the measurement geometry. In case of a double gap geometry, the dimensions of the outer gap are critical, as this is where the vortices

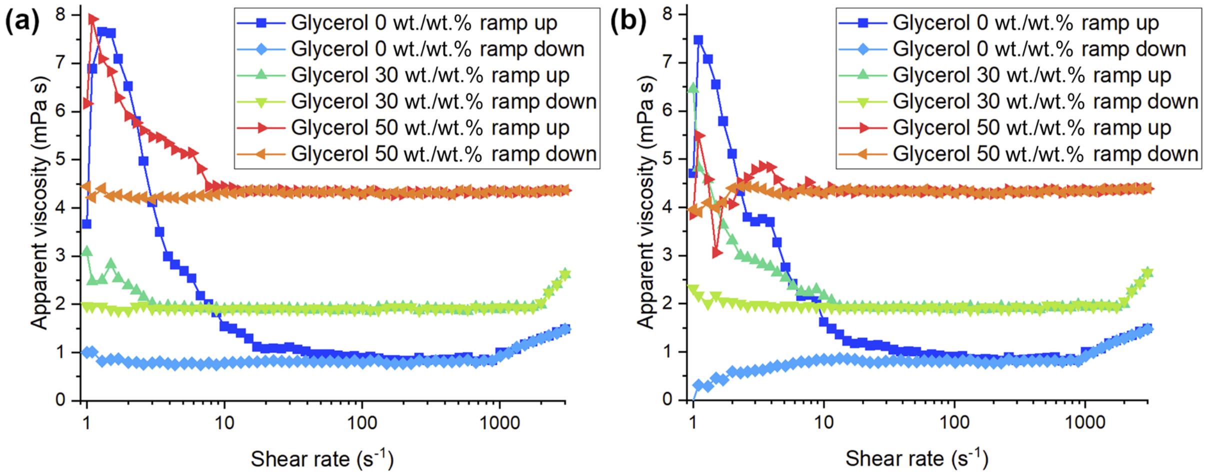

FIG. 2. Results of up-and-down shear ramp segments with selected individual glycerol samples, demonstrating (a) successful removal of contact line asymmetries and (b) artifacts remaining despite the ramping procedures.

first appear. In order to calculate the critical shear rate, the relationship between the shear rate (rheometrical parameter) and the angular velocity (instrument parameter) needs to be known; a representative shear rate $\dot{\gamma}$ provided in the manufacturer's specifications for the employed geometry is presented in the following equation:

$$\dot{\gamma} = \omega \frac{1 + (r_o/r_i)^2}{(r_o/r_i)^2 - 1}, \tag{2}$$

where ω stands for the angular velocity (rad s^{-1}), while r_o and r_i stand, respectively, for the outer and inner radii of the annular gap, i.e., the radius to the inside of the outer wall of the double-walled cup and the radius to the outside wall of the single wall bob. The manifestation of Taylor vortices between concentric cylinders can be predicted with the Taylor number *Ta*, defined in one convenient form in the following equation:

$$Ta = r_i (r_o - r_i)^3 \omega^2 \rho^2 \eta^{-2}, \tag{3}$$

where ρ stands for the density and η stands for the viscosity of the fluid (White, 1999). For narrow gaps, vortices manifest themselves when the critical Taylor number Ta_{crit} is ~1 700, or higher. The critical shear rate $\dot{\gamma}_{\mathrm{crit}}$ corresponding to Ta_{crit} can be then obtained by combining Eqs. (2) and (3), resulting in the following equation:

$$\dot{\gamma}_{\mathrm{crit}} = \frac{\eta}{\rho} \cdot \frac{1 + (r_o/r_i)^2}{(r_o/r_i)^2 - 1} \sqrt{\frac{Ta_{\mathrm{crit}}}{r_i (r_o - r_i)^3}}. \tag{4}$$

For convenience, this can also be written as per the following equation:

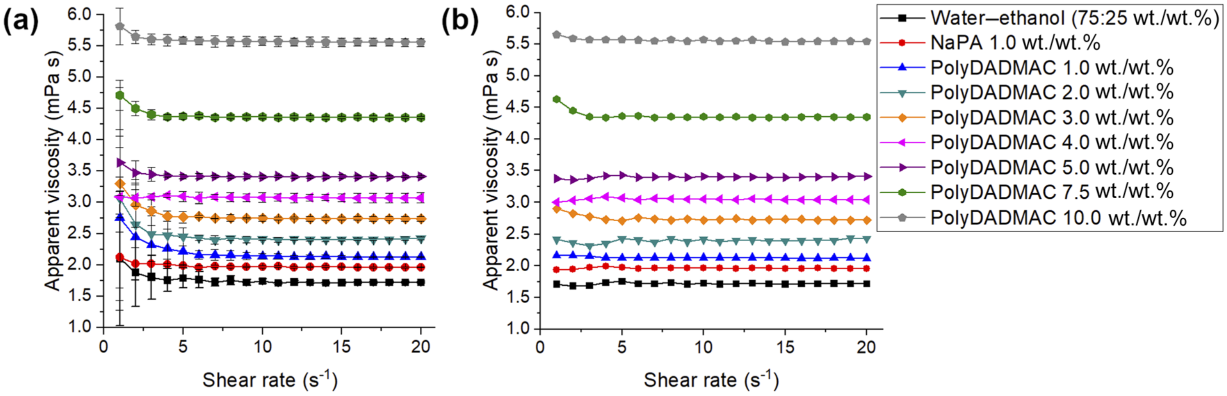

FIG. 3. Measured viscosities of polyelectrolyte solutions at low shear rates, showing (a) average values with 95% confidence intervals, suggesting apparent shear thinning, and (b) select individual measurements demonstrating effectively Newtonian behavior (polyelectrolyte samples with 0.1 wt./wt. %, 0.2 wt./wt. %, and 0.5 wt./wt. % concentrations are omitted for clarity).

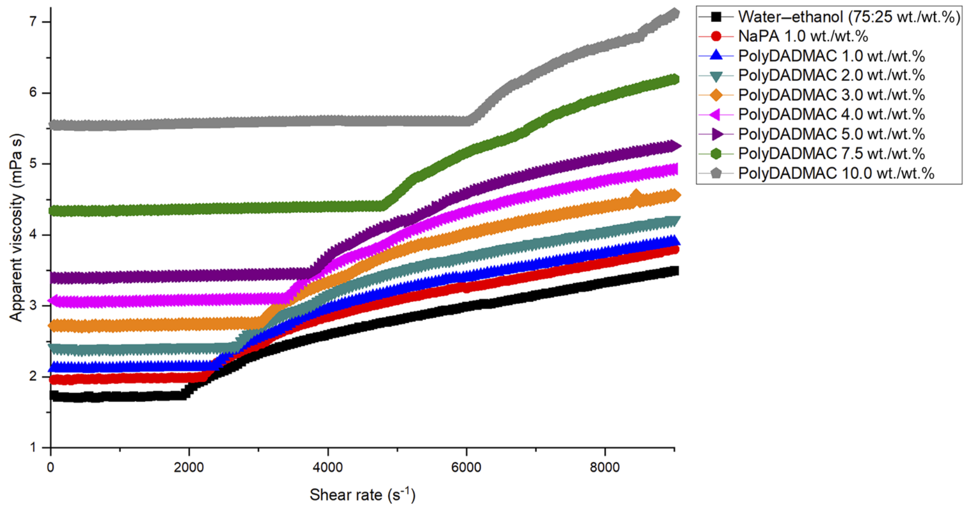

FIG. 4. Measured viscosities of polyelectrolyte solutions at shear rates from 50 s^{-1} to 9000 s^{-1} (confidence intervals and polyelectrolyte samples with 0.1 wt./wt. %, 0.2 wt./wt. %, and 0.5 wt./wt. % concentrations are omitted for clarity).

$$\dot{\gamma}_{\mathrm{crit}} = \frac{\eta}{\rho} \cdot k, \tag{5}$$

where k (arbitrary naming) is a geometry specific coefficient defined from Eq. (4) as

$$k = \frac{1 + (r_{\mathrm{o}}/r_{\mathrm{i}})^2}{(r_{\mathrm{o}}/r_{\mathrm{i}})^2 - 1} \sqrt{\frac{Ta_{\mathrm{crit}}}{r_{\mathrm{i}}(r_{\mathrm{o}} - r_{\mathrm{i}})^3}}. \tag{6}$$

For the outer gap of the double gap geometry in this work, r_{o} equals 13.791 mm, r_{i} equals 13.334 mm, and k equals 1.085×10^9 m^{-2}. The predicted critical shear for the onset of Taylor vortices, shown in Table III and calculated according to Eq. (5) from the respective density and viscosity values, matches well with the experimental results, where an apparent viscosity increase is observed at shear rates slightly above the predicted critical value. An exception is the case of the 60 wt./wt. % glycerol sample, where the increase is already observed at a shear rate slightly under the predicted critical value. While the presence of dissolved polymers can affect manifestation of Taylor vortices (Muller, 2008), no such effect is observable here, with the polyelectrolyte solutions acting like Newtonian fluids.

Measured apparent viscosities of the reference glycerol solutions are shown in Fig. 5. Two glycerol samples, of 70 and 75 wt./wt. %, were of sufficiently high viscosity not to display Taylor vortices in the measured shear rate range, revealing instead another centrifugal artifact in the form of apparent shear thinning, likely due to part of the sample being displaced to the outer edge of the measuring gap.

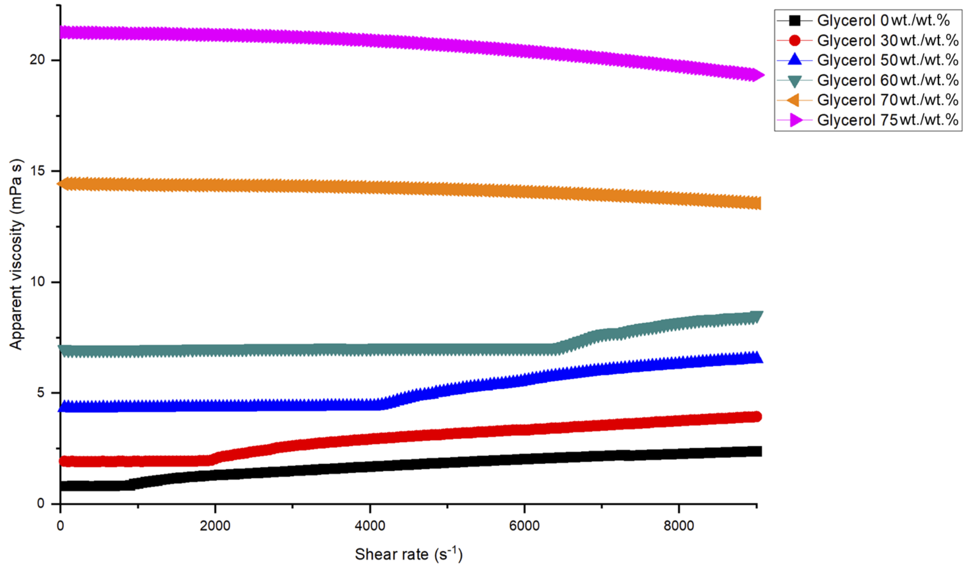

FIG. 5. Apparent viscosity of glycerol solutions as a function of shear rate. Samples with 70 and 75 wt./wt. % demonstrate apparent shear thinning, likely an artifact due to centrifugal displacement of the liquid within the annular gap, while others display Taylor vortices (confidence intervals are omitted for clarity).

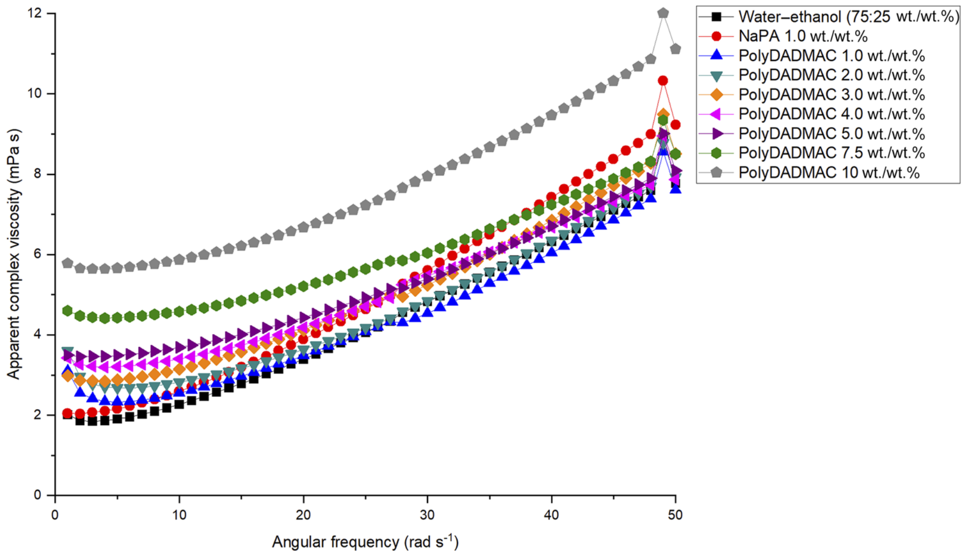

FIG. 6. Apparent complex viscosities (magnitude) of polyelectrolyte solutions as a function of angular frequency (confidence intervals and polyelectrolyte samples with 0.1 wt./wt. %, 0.2 wt./wt. %, and 0.5 wt./wt. % concentrations are omitted for clarity).

Oscillational rheometry studies

Apparent complex viscosities as a function of angular frequency, from rheological measurement segment No. 8, are shown in Fig. 6 for the polyelectrolyte solutions. Due to the inherent difficulty of reliably measuring phase angles at low shear stresses, caused by low signal-to-noise ratios, the magnitude of the complex viscosity, η^* (= $|\boldsymbol{\eta}^*|$), was analyzed rather than the commonly quoted storage and loss moduli parameters.

For a Newtonian fluid, complex viscosity is equal to steady shear viscosity, regardless of the angular frequency. Thus, the results shown in Fig. 6, in which a dependency of complex viscosity on angular frequency seems to be apparent, could naively be assumed to be a sign of non-Newtonian behavior. However, the measurement results for the truly Newtonian reference glycerol solutions, shown in Fig. 7, demonstrate a similar apparent increase in complex viscosity as a function of increasing angular frequency. This behavior of a known Newtonian liquid indicates the presence of an inertial effect, presenting an artifact in the oscillation studies. In this case, it is likely due to inertia (mass acceleration/deceleration) of the measured liquid itself. While the rheometer applies angular momentum compensation to offset instrumental inertia, the inertia of the liquid in the measuring gap can only be dampened by viscous drag loss over time.

While the presence of such artifacts means that the oscillational measurement results are of no direct absolute utility, the polyelectrolyte solutions can be observed to manifest similar artifacts to those of the glycerol samples. Therefore, the initial assumption of

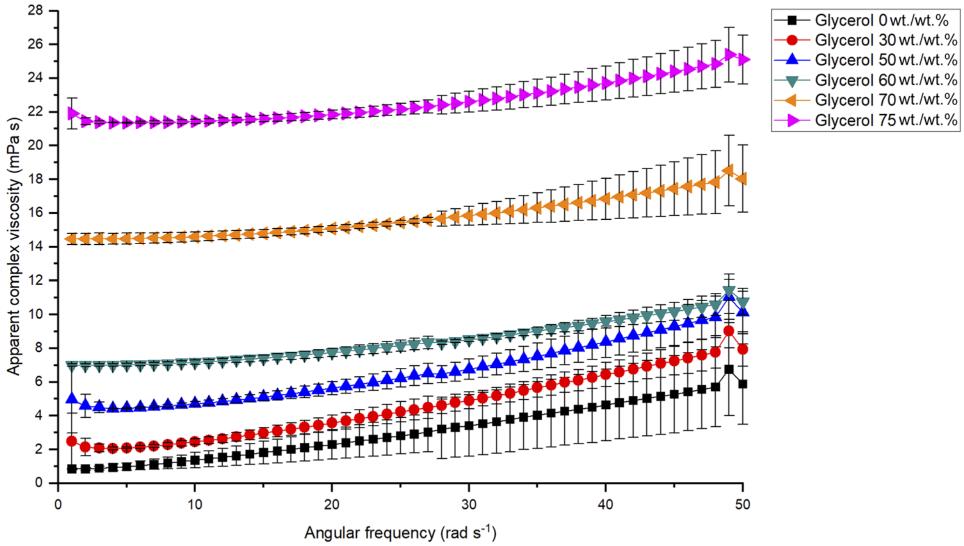

FIG. 7. Apparent complex viscosities (magnitude) of reference glycerol solutions with 95% confidence intervals, with the latter increasing noticeably with increasing angular frequency.

Newtonian behavior for the tested fluids cannot be rejected based on the steady shear or oscillational studies, as long as the presence of artifacts is taken into account. Furthermore, we can conclude that the liquids under test readily display inertia given the specific oscillatory acceleration regime applied.

Limitations of rheometrical characterization

As far as could be reliably tested with the available hardware, the measured samples seem to demonstrate Newtonian behavior. However, the measurement conditions are not truly representative of those encountered in the printhead, where the ink is accelerated over μs timescales, encountering transitionary shear rates of the order of 10^5 $\mathrm{s^{-1}}$ at the nozzle before being ejected from the nozzle with a tailing filament subject to extension. Thus, an ideal experimental setup for inkjet characterization might involve a combination of high shear rate (10^5–10^6 $\mathrm{s^{-1}}$), high frequency oscillation (100–1000 kHz), and extensional rheometry measurements. Under such conditions, the inks studied in this work might indeed display non-Newtonian behavior, though the crucial key point remains the role of inertia, which under extremely high acceleration might lead to inertially induced dilatancy.

As shown previously, oscillational studies with the rotational rheometer manifest liquid inertial artifacts on low viscosity samples already at moderately low angular frequencies. Such artifacts in respect to recovering absolute rheological values cannot be easily removed by instrument design, and even if they could, the maximum frequencies for such mechanical transducers are rather limited: 628 rad $\mathrm{s^{-1}}$ or 100 Hz for the instrument in this work. More specialized methods are required to explore the high frequency regime, such as piezo-axial vibrator and torsion resonator rheometers (Vadillo *et al.*, 2010b).

Unfortunately, the behavior of low viscosity fluids under extension cannot be studied with the available commercial filament thinning rheometer Haake CaBER (Thermo Scientific, Germany) due to asymmetric acceleration combining with liquid inertia effects (Campo-Deano and Clasen, 2010). While alternative experimental methods for studying low viscosity samples under extension have been presented in the literature, such as the slow retraction method with minimal inertia (Campo-Deano and Clasen, 2010), the Cambridge Trimaster dual piston method with symmetric acceleration (Vadillo *et al.*, 2010a), and the dripping-on-substrate method (Dinic *et al.*, 2015), these have not been commercialized to the best of our knowledge.

Jetting characterization

Observed results for the polyelectrolyte jetting studies conducted at 5 kHz jetting frequency are summarized in Table IV. As many of the solutions had similar physical properties, some of the concentrations (0.1 wt./wt. %, 0.2 wt./wt. %, and 4.0 wt./wt. %) were omitted from this part of the study.

Jetting voltage indicates the actuation signal required for the drop to travel ~300 μm distance in 60 μs time. Based on the literature, such as a study with polystyrene solutions (Hoath *et al.*, 2012), the required voltage was expected to increase as the dissolved polymer content increases. However, this was not observed in the present study, with similar actuation voltages required for the water–ethanol mixture (no polyelectrolyte present) and the most concentrated polyDADMAC solutions. At a single cartridge level, variations in the required voltage existed for the individual nozzles, as can be observed from the jetting voltage confidence spread. Since each solution was jetted with a separate unused printhead, manufacturing variations between them may randomly affect the required voltages. While this study could have been alternatively performed with just one single printhead per polyelectrolyte, reducing the variation, it is difficult to predict whether the printhead could have been reliably cleaned after each test.

Early velocity of the ink column head exiting the nozzle can be calculated from the distance traveled between time points 6 μs

TABLE IV. Jetting results at 5 kHz frequency and maximum stable jetting frequency. All times are given in relation to the start of the jetting cycle. Values are reported with 95% confidence intervals.

		Velocity		Tail filament		Satellite droplet(s)			
Sample	Jetting voltage (V)	Early ($\mathrm{m\,s^{-1}}$)	Final ($\mathrm{m\,s^{-1}}$)	Detachment time (μs)	Merge time (μs)	Break-off time (μs)	Merge time (μs)	Maximum stable frequency (kHz)	Maximum idle time (s)
Water–ethanol	19.5 ± 1.7	7.0 ± 0.0	4.7 ± 0.2	19 ± 0	NA	26 ± 0	45 ± 12	9.4	900
NaPA 0.5 wt./wt. %	15.2 ± 1.3	6.8 ± 0.8	4.7 ± 0.3	19 ± 3	NA	27 ± 3	41 ± 8	9.4	900
NaPA 1.0 wt./wt. %	18.5 ± 1.2	7.3 ± 1.0	4.7 ± 0.2	20 ± 0	NA	28 ± 2	43 ± 3	10.5	900
PolyDADMAC 0.5 wt./wt. %	17.4 ± 1.1	6.8 ± 0.5	4.7 ± 0.2	20 ± 0	NA	29 ± 0	42 ± 2	9.4	300
PolyDADMAC 1.0 wt./wt. %	17.1 ± 1.5	6.8 ± 1.0	4.8 ± 0.3	22 ± 0	43 ± 2	NA	NA	9.4	300
PolyDADMAC 2.0 wt./wt. %	17.7 ± 1.8	7.0 ± 0.7	4.5 ± 0.2	22 ± 0	NA	31 ± 1	40 ± 4	9.4	60
PolyDADMAC 3.0 wt./wt. %	18.6 ± 0.5	7.2 ± 0.5	4.7 ± 0.2	23 ± 1	NA	36 ± 0	48 ± 3	10.5	60
PolyDADMAC 5.0 wt./wt. %	19.3 ± 0.5	7.3 ± 0.8	4.6 ± 0.2	23 ± 0	NA	38 ± 0	47 ± 2	10.5	20
PolyDADMAC 7.5 wt./wt. %	19.0 ± 0.2	6.6 ± 1.3	4.6 ± 0.2	24 ± 0	46 ± 0	NA	NA	10.5	10
PolyDADMAC 10.0 wt./wt. %	19.0 ± 1.0	7.6 ± 0.5	4.6 ± 0.1	25 ± 0	47 ± 2	NA	NA	10.5	5

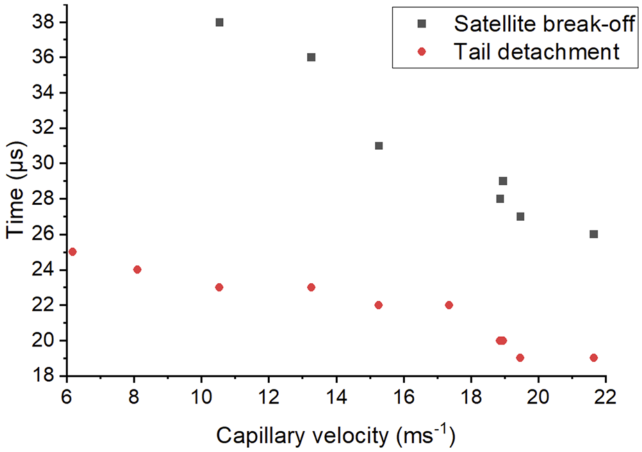

FIG. 8. Times for tail detachment and satellite break-off at 5 kHz jetting frequency as a function of capillary velocity. Confidence intervals are not displayed.

and 12 μs, partially illustrating the early stage rapid motion. Past this point, the head decelerates to a velocity close to the drop final velocity, which can be calculated from the distance traveled between time points of 60 μs and 200 μs (60 μs and 135 μs in the case of 7.5 wt./wt. % polyDADMAC due to the limited observation window). As intended, the measured final velocities are quite similar for all the tested solutions and are just under the manufacturer recommended (rule of thumb) velocity range of 5–10 m s^{-1}. An experimental minimum velocity of 2 m s^{-1} has been reported for a variety of water, isopropanol, and ethylene glycol mixtures with the same printhead (Wong *et al.*, 2012). Employing significantly higher velocities would have limited the time window available for observing tail/satellite behavior. At the early high velocity stage, the imaging system resolution results in high confidence intervals, as the distance traveled in the 6 μs timeframe is at most equivalent to 18 pixels on the recorded images.

Tail detachment time indicates the time point where the trailing ligament of the drop could be clearly observed as having detached from the nozzle. This value sets a theoretical limit for the jetting frequency, as the actuation cycle for the deposition of the next drop should not start before the previous one has detached completely from the nozzle. Based on the literature (Dong *et al.*, 2006), this value was expected to increase as a function of viscosity. The ligament thinning leading to detachment is driven by surface tension, varying only slightly for the tested polyelectrolyte solutions, and resisted by viscosity. Figure 8 demonstrates the relationship between the time points for tail detachment and satellite break-off with capillary velocity $\sigma\eta^{-1}$, a parameter frequently employed in filament thinning studies. Unfortunately, the imaging setup does not have sufficient resolution for reliable measurement of actual filament widths, enabling deeper analysis.

Jetting frequency

Besides tail detachment time, another factor affecting the maximum practical jetting frequency is the time required for viscous damping of the remnant acoustic wave caused by the previous actuation within the printhead (Wijshoff, 2010). Based solely on the tail detachment times, maximum jetting frequencies of 40–50 kHz could be expected. However, as the jetting frequency was increased from the initial value of 5 kHz, unstable jetting was observed already at lower frequencies, initially in the form of what appeared to be wobbling in drop velocities. Maximum stable frequency was arbitrarily determined by selecting the highest frequency at which the wobbling was not noticeable. This frequency was expected to increase with increasing viscosity, but the observable effect was minor: 10.5 kHz for the samples with viscosity ≥2.7 mPa s and 9.4 kHz for the samples with lower viscosity, with the exception of NaPA 1.0 wt./wt. % for which the maximum stable frequency of 10.5 kHz was recorded, despite having a viscosity of 1.96 ± 0.02 mPa s.

As the jetting frequency increased, but already before wobbling manifested, changes in steady drop velocity were observed alternatingly after 0.9 kHz and 1.1 kHz increments with all samples (specifically at 5.5 kHz, 6.6 kHz, 7.5 kHz, 8.6 kHz, 9.5 kHz, 10.6 kHz, 11.5 kHz, 12.6 kHz, 13.5 kHz, 14.6 kHz, 15.5 kHz, and 16.6 kHz). When lower frequencies were later tested with 1.0 wt./wt. % NaPA solution, similar effects were also observed at 3.5 kHz and 4.6 kHz, complementing the observed pattern. Such frequency-dependence is due to internal channel acoustics and reflection/resonance of the initial pulse within the printhead. Since the pulse is affected by viscous damping within the ink channels, the effects are expected to be most pronounced for low viscosity samples.

Figure 9 illustrates the variation in jetting behavior for 2.0 wt./wt. % and 7.5 wt./wt. % polyDADMAC inks over a range of jetting frequencies. In the case of the low viscosity 2.0 wt./wt. % polyDADMAC ink, variation in both satellite droplet formation and drop velocity is clearly observable, while for the higher viscosity 7.5 wt./wt. % polyDADMAC ink, only very minor variations can be observed. The velocity variation is observed most easily from the drop location at the 60 μs travel point, corresponding to roughly 300 μm travel distance.

Satellite droplet formation

Formation of the trailing satellite droplet(s) was observed on most samples at 5 kHz jetting frequency, though the location where the satellite droplet formed varied. The following regimes, listed in the order of descending Oh^{-1}, could be observed:

(i) end-pinching, where the satellite droplet forms as the end of the tail pinches off, while the rest of the tail pulls up with the main drop (water–ethanol, polyDADMAC 0.5 wt./wt. %, and NaPA 0.5 and 1.0 wt./wt. %),
(ii) no satellites (polyDADMAC 1.0 wt./wt. %),
(iii) multiple-pinching, where the tail pinches off at both ends, resulting in two satellite drops (polyDADMAC 2.0 wt./wt. %),
(iv) front-pinching, where the whole tail pinches off (polyDADMAC 3.0 and 5.0 wt./wt. %), and
(v) no satellites (polyDADMAC 7.5 wt./wt. % and 10 wt./wt. %).

In all cases, the satellite droplets traveled at a higher velocity than the main droplet, resulting in their re-merging with the main droplet. The times for the break-off and re-merging of the satellite droplets are displayed in Table IV, while Fig. 8 shows the

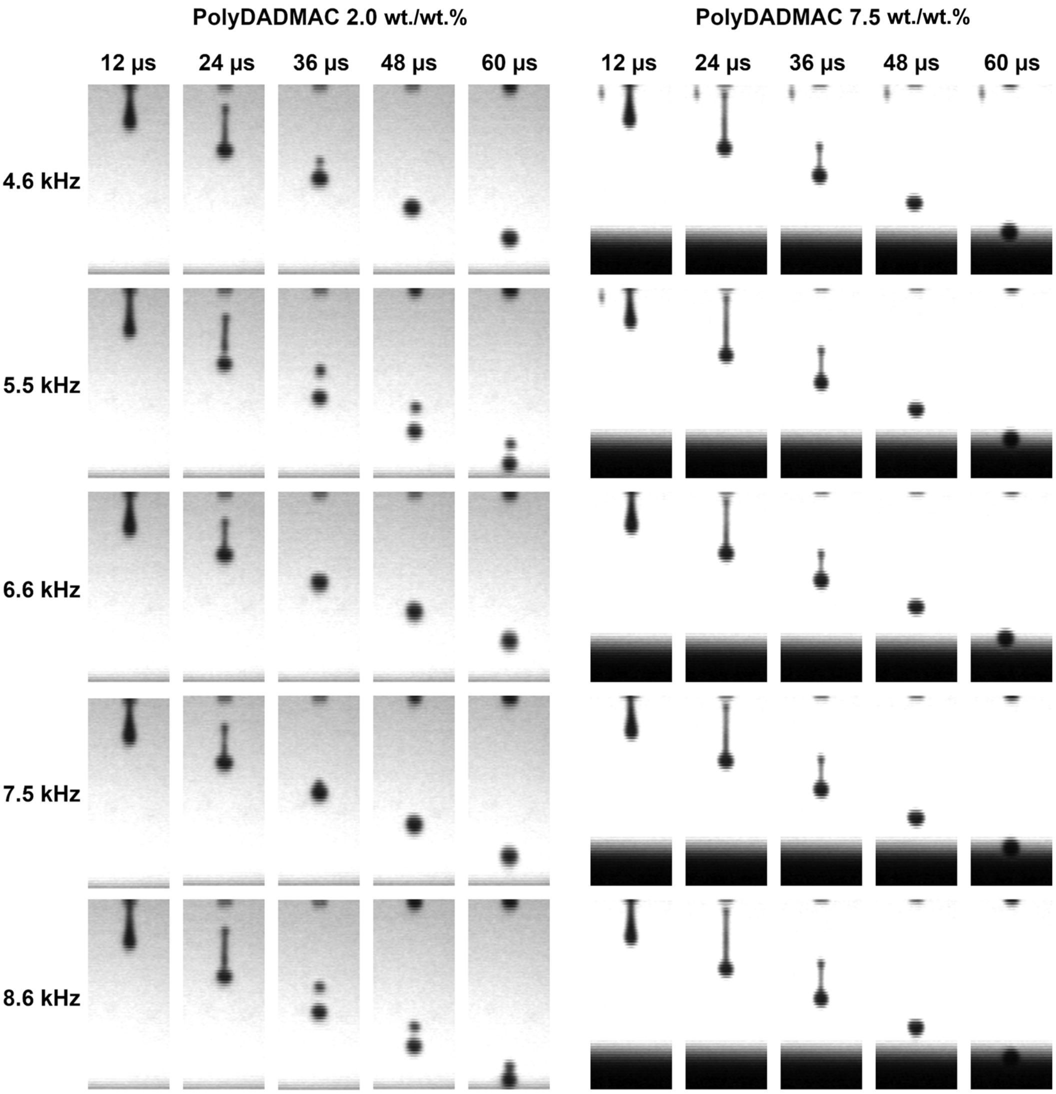

FIG. 9. Jetting behavior of 2.0 kHz and 7.5 kHz polyDADMAC inks as a function of jetting frequency from 4.6 kHz to 8.6 kHz.

break-off time as a function of capillary velocity. For the samples where no satellite droplet(s) emerged, the time for the trailing filament to merge completely is reported in Table IV; where the satellite droplet(s) were present, this time for complete merging could not be determined unambiguously. In all cases, the trailing filament and/or satellite droplets had formed into a single spherical droplet within 50 μs.

While many published studies report results over a single continuous range of Oh^{-1}, for which no satellite droplet formation is observed, such behavior is not observable here, as the regimes (ii) and (v) where no satellite droplets are manifested are discontinuous. Furthermore, satellite droplet formation is also dependent on jetting parameters and resulting ink column velocity, which is not accounted for in the Ohnesorge number. Alternatively, filament break-off into satellites can also be approached in terms of the Ohnesorge number and filament aspect ratio (Hoath *et al.*, 2013b), if the imaging setup resolution enables accurate measurement of the initial filament width, which again is likely dependent on jetting parameters and ink properties.

Idle times and evaporation effects

The observed maximum idle time, after which jetting could still be activated, varied greatly, as shown in Table IV. In the case of water–ethanol and NaPA samples, jetting would still commence after the longest observed break of 900 s. However, in the case of samples containing polyDADMAC, this time radically decreased from 300 s to merely 5 s as the polyelectrolyte content increased from

1 wt./wt. % to 10 wt./wt. %. This phenomenon can be explained by local solvent evaporation at the nozzles, resulting in an increase in surface tension and/or viscosity compared to those of the bulk liquid, which cannot be sufficiently counter-acted by the tickle pulse, defined by the non-jetting waveform segments in Table II.

In most cases, the nozzles that had become non-jetting while idle could be easily recovered into a jetting state by employing an over-pressure cleaning function ("purge" in instrument-specific terminology) to force ink out of the nozzle. However, with polyDADMAC concentrations of 5 wt./wt. % or more, jetting at some of the nozzles was observed as either not recovered or misdirected; this may be due to the earlier jetting failure, which may have resulted in air imbibition within the nozzle (preventing further jetting) or remnants of deposited inks on the nozzle plate around the nozzle exit (causing misdirected jetting). The problem was most significant with 7.5 wt./wt. % and 10 wt./wt. % polyDADMAC solutions, where many nozzles became non-jetting already in the initial phase of determining suitable jetting voltages, and therefore, jetting evaluation had to be conducted with two and three nozzles, respectively, instead of five nozzles as for other samples.

Directly measuring the local surface tension or viscosity at the nozzle is not possible with the employed instrumentation. However, it is possible to calculate rough estimates of how large such an increase would need to be to affect jetting behavior. Therefore, in the following, the potential effects of local increase in surface tension and viscosity are independently modeled.

Effects of local surface tension increase

Since the inks in this study contain two carrier liquids, water and ethanol, faster relative evaporation of ethanol at the nozzle would result in a local surface tension increase, thus requiring more kinetic energy to be consumed to produce a new droplet. The energy of a newly generated drop can be divided into kinetic energy E_K and total drop surface energy E_S, defined as

$$E_K = 0.5mv^2 = 0.5\rho V v^2, \tag{7}$$

$$E_S = 4\pi r^2 \sigma = (36\pi)^{1/3} \sigma V^{2/3}, \tag{8}$$

where ρ and σ, as before, are the fluid density and surface tension, respectively, while m, v, r, and V indicate the drop mass, velocity, radius, and volume, respectively.

While the exact drop volumes for the different inks in this study were not measured, they can be expected to be comparable to the nominal 10 pl drop volume. Figure 10 displays the kinetic and surface energies calculated for a range of representative drops of varying volumes, velocities, and surface tensions, with an assumed density of 980 kg m^{-3}. The selected surface tension values of 35 mN m^{-1}, 47 mN m^{-1}, 55 mN m^{-1}, and 71 mN m^{-1} correspond to values reported for 25 wt./wt. %, 10 wt./wt. %, 5 wt./wt. %, and 0 wt./wt. % aqueous ethanol solutions at 30 °C, respectively (Vasquez *et al.*, 1995).

As can be seen from Fig. 10, these drop volumes, velocities, and surface tensions are in a crossover region, where the kinetic and drop total surface energies are of a very similar magnitude, and in some cases equal, e.g., for a 10 pl drop with a velocity of 4 m s^{-1} and surface tension of 35 mN m^{-1}. The actual kinetic energy already consumed to overcome surface tension and form a new drop is likely higher than the actual surface energy of the final drop, as in the intermediate stages of drop formation the combined surface area of the drop head and the tailing filament is larger than the surface area of the final drop.

The jetting settings in this study were deliberately designed to produce drop velocities of no more than 5 m s^{-1} with bulk liquid drops. Thus, if over an idle period the local surface tension of the ink at the nozzle exit was to increase close to that of pure water, the ink column exiting the nozzle might not have sufficient kinetic energy to overcome the increased surface tension and form a discrete drop. Instead, ink would be pumped out of the nozzle and flood the surrounding nozzle plate, as was observed to take place in many cases when nozzles were activated after an idle period. In this case, adjustment of jetting settings, to generate a higher velocity, and, therefore, kinetic energy to the exiting fluid, could provide a cure for overcoming the increased surface tension. Thus, the non-jetting problem might be reduced into the so-called *first drops problem*, where the

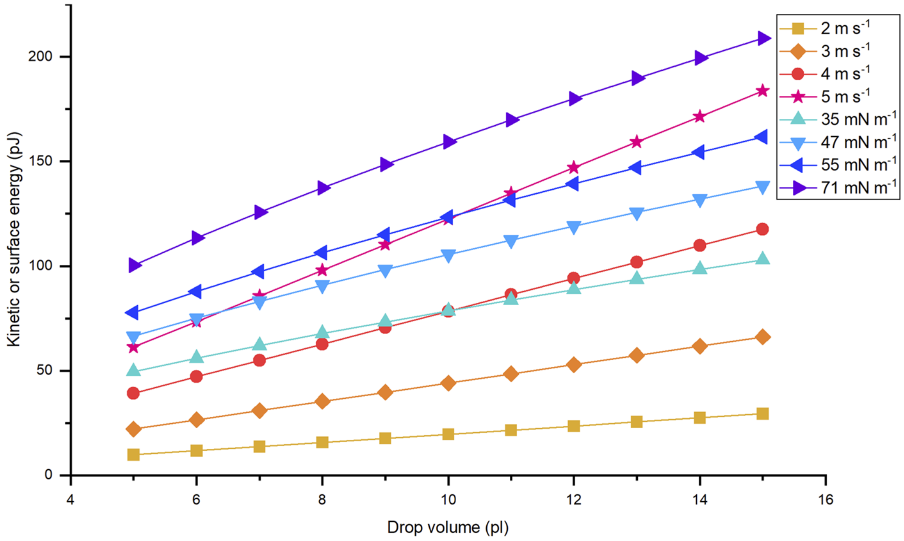

FIG. 10. Kinetic energy for various drop velocities (2–5 m s^{-1}) and total drop surface energy for various ink surface tensions (35–71 mN m^{-1}) as a function of drop volume for hypothetical drops with a density of 980 kg m^{-3}.

first drops after activation simply have differing velocities compared to the bulk drops.

While all of the experimented inks in this work contained similar amounts of ethanol (25 wt./wt. %), they were not all equally affected by the evaporation, with the water–ethanol and NaPA inks still jetting after 900 s idle time. The jettability of the polyDADMAC inks was more susceptible to evaporation, suggesting that, in their case, there was a likely local viscosity increase as a function of increased concentration at the nozzle exit. This could act to slow down the diffusion of ethanol from the bulk liquid to the surface, thus affecting how the surface tension changes over time and/or contributes to an increase in the viscous damping within the printhead—the latter possibility forms the basis for discussion in the section titled Effects of local viscosity increase and inertia.

Effects of local viscosity increase and inertia

Estimating the effects of viscous damping within the printhead requires a number of assumptions and simplifications. With a basic fluid mechanics model, the pressure exerted by the piezoelectric element has to overcome steady and unsteady inertia, viscous losses, and capillary pressure to accelerate and eject ink from the nozzle with sufficient velocity (Wijshoff, 2010). Inertial and viscous losses can be represented as pressure components, dependent on fluid properties and internal printhead geometries.

Unfortunately, no information is available from the manufacturer regarding the printhead geometries, or the pressure and displacement profiles for the piezoelectric element. However, a cross-sectional SEM image of the printhead has been published (Li *et al.*, 2018). This displays a pump chamber, with an ~100 μm wide and 500 μm long ink channel leading into a triangular cross-sectional exit channel, tapering from 65 μm initial width into 21.5 μm exit width over a length of 30 μm. While the height of the channels is not apparent from the published image, it can be reasonably assumed that the channel cross sections are square in profile, i.e., equal in height and width. Figure 11 shows a simplified schematic of this geometry.

For estimating the effects of increased viscous damping in the printhead due to evaporation, the pressure applied by the piezoelectric element stimulated with a fixed jetting profile can be assumed to remain constant. Furthermore, if only ink viscosity is assumed to change, then the capillary pressure at the nozzle can be assumed to remain constant, as well as the backpressure exerted by meniscus vacuum and gravity. For calculating viscous losses, laminar flow is taken as the approximation.

The pressure components that the piezoelectric actuation needs to overcome are steady inertia p_{si} in Eq. (9), based on Bernoulli pressure, unsteady inertia p_{ui} based on Newton's second law, and given for the assumed uniform section in Eq. (10), and viscous loss p_v based on the Hagen–Poiseuille flow, and given for the same uniform section in Eq. (11),

$$p_{si} = 0.5\rho v_{max}^2, \tag{9}$$

$$p_{ui} = \frac{\rho l v}{t_{rise}}, \tag{10}$$

$$p_v = \frac{8\eta l Q}{\pi r^4}, \tag{11}$$

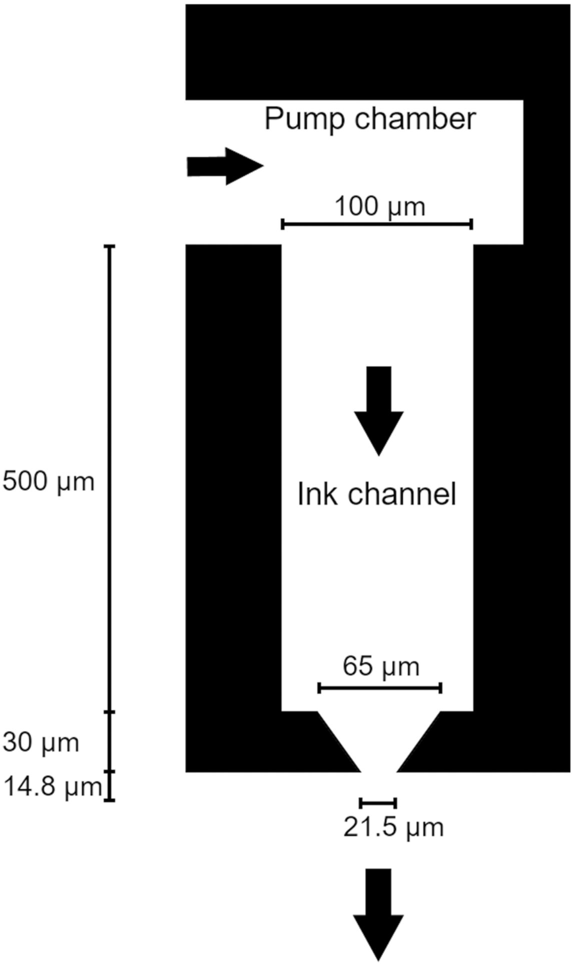

FIG. 11. Schematic illustration of the printhead structure (not to scale) assumedly having a square channel cross section; arrows indicate the direction of the ink flow (after Li *et al.*, 2018).

where ρ and η stand for the fluid density and viscosity, respectively, v and v_{max} stand for local and maximum fluid (representative) velocities, respectively, l and r stand for the length and radius of the channel, respectively, t_{rise} stands for the piezoelectric element rise time, and Q stands for the volume flow rate in the channel (Wijshoff, 2010). Since the channel cross section has been assumed to be square, r becomes the hydraulic radius r_H, which for the square cross section is half of the channel width a. The combined inertial–viscous pressure p_{iv} resisting the actuation can be expressed as a sum as per the following equation:

$$p_{iv} = p_{si} + p_{ui} + p_v. \tag{12}$$

Since in the present case the ink channel consists of two sections, the first with a uniform cross section and the second with a tapering cross section, Eqs. (9)–(11) need to be re-formulated, with the pressure effects for the tapering pyramidal section calculated by integration. To assist in this work, conservation of volume provides the following equations:

$$Q = vA, \tag{13}$$

$$v = \frac{v_{\text{exit}} A_{\text{exit}}}{A}, \tag{14}$$

where A stands for the channel cross-sectional area, A_{exit} stands for the nozzle exit cross-sectional area ($21.5 \times 21.5\ \mu\text{m}^2$), and v_{exit} stands for the fluid velocity at the nozzle exit. For the present geometry, $v_{\max}$ equals v_{exit}. Re-formulated geometry-specific versions of the pressure components are given in the following equations:

$$p_{\text{si}} = 0.5\rho_2 v_{\text{exit}}^2, \tag{15}$$

$$p_{\text{ui}} = \frac{v_{\text{exit}} A_{\text{exit}}}{t_{\text{rise}}} \left(\frac{\rho_1 l_1}{A_1} + \rho_2 \int_{l_{\text{exit}}}^{l_{\text{start}}} \frac{1}{A(l)} \mathrm{d}l \right), \tag{16}$$

$$p_{\text{v}} = \frac{128 v_{\text{exit}} A_{\text{exit}}}{\pi} \left(\frac{\eta_1 l_1}{A_1^2} + \eta_2 \int_{l_{\text{exit}}}^{l_{\text{start}}} \frac{1}{A(l)^2} \mathrm{d}l \right), \tag{17}$$

where l_1 and A_1 stand for the length and cross-sectional area of the uniform channel section, l_{exit} and l_{start} stand for locations of the exit and entry of the tapering channel section, respectively, ρ_1 and ρ_2 stand for densities in the uniform and tapering channel sections, respectively, and η_1 and η_2 stand for viscosities in the uniform and tapering channel sections, respectively. Assuming uniform viscosity distribution in the tapering channel section after evaporation is a simplification for practical modeling purposes, and a more detailed model could account for viscosity gradient, though the possible effect of the tickle pulse in promoting mixing, and thus supporting largely uniform viscosity, in this region should not be ignored.

For solving the integrals in Eqs. (16) and (17), the cross-sectional area of the pyramidal tapering channel can be expressed as per the following equation:

$$A(l) = 2.1025 l^2, \tag{18}$$

where l stands for the distance from the (imaginary) tip of the pyramid, with $l_{\text{exit}} = 1290/87\ \mu\text{m} \approx 14.8\ \mu\text{m}$ and $l_{\text{start}} = l_{\text{exit}} + 30\ \mu\text{m} = 3900/87\ \mu\text{m} \approx 44.8\ \mu\text{m}$. Inserting Eq. (18) into Eqs. (16) and (17), solving the integrals, and re-organizing the terms result in the following equations:

$$p_{\text{ui}} = v_{\text{exit}} \left[\rho_1 \left(\frac{A_{\text{exit}} l_1}{A_1 t_{\text{rise}}} \right) + \rho_2 \left(\frac{A_{\text{exit}}}{2.1025 t_{\text{rise}}} \right) \left(\frac{1}{l_{\text{exit}}} - \frac{1}{l_{\text{start}}} \right) \right], \tag{19}$$

$$p_{\text{v}} = v_{\text{exit}} \left[\eta_1 \left(\frac{128 A_{\text{exit}} l_1}{\pi A_1^2} \right) + \eta_2 \left(\frac{128 A_{\text{exit}}}{3(2.1025)^2 \pi} \right) \left(\frac{1}{l_{\text{exit}}^3} - \frac{1}{l_{\text{start}}^3} \right) \right]. \tag{20}$$

Inserting numerical values for A_{exit}, A_1, l_1, l_{exit}, l_{start}, and t_{rise}, the pressure components can be expressed in terms of viscosity, density, and exit velocity as per the following equations:

$$p_{\text{ui}} = v_{\text{exit}} \left[\rho_1 \left(9.6302\ \text{ms}^{-1} \right) + \rho_2 \left(4.1346\ \text{ms}^{-1} \right) \right], \tag{21}$$

$$p_{\text{v}} = v_{\text{exit}} \left[\eta_1 \left(94\,169\ \text{m}^{-1} \right) + \eta_2 \left(419\,879\ \text{m}^{-1} \right) \right], \tag{22}$$

which, when reduced to two significant figures, to reflect the uncertainties, become the following equations:

$$p_{\text{ui}} = v_{\text{exit}} \left[\rho_1 \left(9.6\ \text{ms}^{-1} \right) + \rho_2 \left(4.1\ \text{ms}^{-1} \right) \right], \tag{23}$$

$$p_{\text{v}} = v_{\text{exit}} \left[\eta_1 \left(94\,000\ \text{m}^{-1} \right) + \eta_2 \left(420\,000\ \text{m}^{-1} \right) \right]. \tag{24}$$

According to Eq. (23) for unsteady inertia, the straight channel section is dominant, while Eq. (24) indicates that the viscosity in the tapering channel section is the dominant part leading to viscous damping, rather than the bulk liquid in the straight channel.

For estimating the effects of evaporation in the printhead, p_{iv} is assumed to remain constant, as the piezoelectric element will continue to exert similar pressure under constant jetting settings. Thus, if η_2 increases due to evaporation at the nozzle, then v_{exit} must be reduced for p_{iv} to remain constant. Unfortunately, v_{exit} for the steady jetting situation cannot be determined with the present setup, though published simulations for some other printhead and ink combinations have estimated initial tip velocities that are up to twice the final drop velocity (Hoath *et al.*, 2013a), the difference being explainable by the kinetic energy losses for overcoming surface tension.

A hypothetical drop with steady jetting properties of $v_{\text{exit}} = 9$ m s^{-1}, $\rho_1 = \rho_2 = 970$ kg m^{-3}, and $\eta_1 = \eta_2 = 5$ mPa s would have p_{iv} of ∼1.8 bar, which does not sound unreasonable for a printhead piezoelectric element. If a break in jetting takes place during which η_2 increases, while densities and η_1 remain constant, then re-activating the jetting with the same pressure will result in reduced v_{exit}, with, for example, η_2 values of 12 mPa s, 21 mPa s, 32 mPa s, and 48 mPa s corresponding to v_{exit} values of 8 m s^{-1}, 7 m s^{-1}, 6 m s^{-1}, and 5 m s^{-1}, respectively. Thus, the exiting ink column will have significantly less kinetic energy to overcome surface tension, which may lead to non-jetting behavior.

Further examining the different pressure components shows that, for the hypothetical 5 mPa s viscosity ink at 9 m s^{-1} velocity, p_{v} equals ∼0.2 bar, while for the similar 2 mPa s ink, it would be merely 0.1 bar, i.e., in both cases, the inertial components are dominant in determining the required pressure. This explains why there were no practical differences in the voltages required to jet the different inks, as displayed in Table IV; assuming that the applied pressure is directly related to voltage, the required pressure difference might be merely of the order of 1 V, thus getting masked by the manufacturing variation between the individual nozzles and printheads.

In the present work, the effects of evaporation on surface tension and viscosity were modeled separately, as either of these alone could potentially lead to non-jetting behavior. Actually, both of these changes may be taking place simultaneously, and a more complete model should account for both of them at the same time, though such a model is beyond the scope of the present work. However, even these simplified separate models show that the jetting behavior is affected strongly by the local ink properties encountered in the printhead nozzle region, which may, due to evaporation, differ from the respective bulk ink characteristics.

Practical implications

All of the studied solutions formed a single spherical droplet with a velocity ≥4.5 ms^{-1} within 50 μs time and 300 μm travel distance when jetted at 5 kHz frequency, with relatively stable jetting possible up to 9.4 kHz or 10.5 kHz frequency. While temporary satellite droplets are produced with the tested jetting settings, they will not have a practical effect on the printed pattern as long as the stand-off distance between the printhead and the substrate is ≥300 μm. For comparison, the default recommended stand-off distance for the employed printer is 1000 μm. Short stand-off distances and high drop velocities provide more accurate drop placement on the substrate, as the drops have shorter flight times and thus are less affected by local air currents. However, on uneven substrates, short stand-off distances can risk contact between the substrate and the nozzle plate. The observed maximum stable jetting frequencies are significantly below the printhead maximum of 80 kHz.

Possibly, the most important practical parameter observed is the maximum idle time, though this depends on the printing system employed, as well as on the jetting parameters. On the kind of research printer employed in this work, where no capping mechanism exists to prevent evaporation, and where nozzles remain idle for a significant period of time, e.g., between visual inspection of nozzles and start of printing, allowable idle times ≥60 s would be recommendable for the practical research work. Therefore, the practical limit for polyDADMAC solution concentration would likely be somewhat above 3.0 wt./wt. %. However, since the cause of the observed non-jetting behavior is assumed to be insufficient kinetic energy to overcome surface tension after evaporation at the nozzles, adjusting jetting settings to impart higher kinetic energy to the ink column exiting the nozzles would likely result in increased jetting robustness in regard to evaporation. The most important parameter to adjust would be jetting voltage, which is assumed to be directly related to the pressure applied by the piezoelectric element.

Other print setups can be less affected by the local solvent evaporation at the nozzles due to their design. Drop-on-demand printheads with circulating printheads continuously replace the ink at the nozzles with bulk ink, thus reducing the effect of evaporation (Hirakata *et al.*, 2014), while designs with fast capping systems could limit the time exposed to evaporation. Trying to eliminate the evaporation by operating the printhead in a solvent-saturated atmosphere is likely not practicable. In the case of continuous inkjet systems, nozzles are never idle, though since most of the deposited drops are recycled, the bulk ink properties may shift over time due to evaporation.

In the existing literature, the effect of idle times on nozzle jetting has been most often explored in the context of the first drop(s) problem, where the effect of even very short idle times on model inks is explored with high frequency camera setups capable of determining individual drop properties, such as velocity. However, in practical research on new functional ink formulations, the limits of allowable idle times are rarely reported, even though a maximum idle time test, such as the one in this study, is simple and relatively quick to perform. While the results of such studies will be specific to the jetting settings and environment, they can provide one with a rough estimate on the robustness of the ink, likely of major interest for upscaling.

Limitations of jetting characterization

The integral DMP-2831 camera setup, though convenient, has a limited spatial observation window and optical resolution and features a stroboscopic system instead of a high-speed camera. This prevents, for example, reliable measurement of drop volumes, filament widths, or velocity variation between individual drops. Only limited information was available about the internal geometry of the printhead, and no information at all regarding the pressures and displacement volumes of the piezoelectric element. Finally, the DMC-11610 cartridges employed in this study have been discontinued by the manufacturer in autumn 2019, with a replacement product with possibly differing jetting characteristics to arrive onto the market in 2020.

As regards evaporation at the nozzles, being able to measure actual changes in ink physical properties and component concentrations would help in understanding the actual physical effects lying behind the limitation of allowed idle times. Previously, application of non-jetting probe pulses to the nozzle and evaluating the viscous damping of the resulting meniscus motion, monitored with a laser Doppler vibrometer, has been demonstrated as a viable method for measuring local ink viscosity at the nozzle up to 60 mPa s (Seo *et al.*, 2011). Furthermore, a self-sensing printhead design has been demonstrated for viscosity measurements inside a printhead, detectable through changes in probe pulse damping times (Kwon *et al.*, 2013).

CONCLUSIONS

This study characterized physical properties of low molecular weight NaPA and polyDADMAC solutions of various concentrations in the water–ethanol mixture, and their jetting behavior from an inkjet printhead. In steady shear rotational viscosity measurements at accessible shear rates, the tested solutions demonstrated Newtonian behavior, while reliable oscillational rheometry studies were not feasible due to liquid inertia effects. Ink viscosity was found to increase slowly with an increase in polyelectrolyte concentration.

NaPA solutions studied in this work were limited to ≤1.0 wt./wt. % polyelectrolyte, due to poor miscibility of NaPA with aqueous ethanol solutions. Studying NaPA solutions with higher concentrations would require a different solvent system than that employed in this study. PolyDADMAC solutions could be prepared and jetted at least up to 10 wt./wt. % polyelectrolyte content under steady jetting conditions.

The required jetting voltage, to eject drops of different inks at equal velocities, was found to be rather similar for all of the tested inks, instead of increasing with viscosity as originally expected. However, simple models of the jetting pressures suggested that, with low viscosity inks, as studied here, the ink inertia is the dominant factor in resisting acceleration, and the effects of viscosity were minor enough to be disguised by manufacturing variation between individual cartridges and nozzles. Similarly, maximum observed stable jetting frequency increased only slightly, from 9.4 kHz to 11.5 kHz, as ink viscosity increased. Times for drop detachment and satellite droplet formation, if present, expectedly increased as a function of viscosity. No clear criteria could be set to predict manifestation of satellite droplets, though when present they merged with the main drop so quickly as to have no practical effect.

Limitations of the inks in practice were discovered when steady jetting was interrupted, leaving the nozzles idle and exposed to evaporation. In case of NaPA solutions, jetting could be re-activated after idle times up to 900 s. However, with polyDADMAC inks, as the polyelectrolyte concentration increased, the jetting stability of the nozzles became increasingly affected by the evaporation at idle nozzles, where solvent evaporation results in a local increase in surface tension and/or viscosity. This demonstrates that the jetting behavior cannot be purely predicted based on the bulk physical properties of the ink when volatile solvents are employed. However, due to the length scales involved, analysis of the local composition or physical properties of the surface ink layer at the exposed nozzle remains challenging compared to that of the bulk properties.

ACKNOWLEDGMENTS

This work made use of Aalto University Bioeconomy Facilities. This project was fully funded by Omya International AG (Oftringen, Switzerland).

DATA AVAILABILITY

The data that support the findings of this study are available from the corresponding author upon reasonable request.

REFERENCES

Campo-Deaño, L. and Clasen, C., “The slow retraction method (SRM) for the determination of ultra-short relaxation times in capillary breakup extensional rheometry experiments,” J. Non-Newton Fluid Mech. **165**, 1688–1699 (2010).

Cardinaels, R., Reddy, N. K., and Clasen, C., “Quantifying the errors due to overfilling for Newtonian fluids in rotational rheometry,” Rheol. Acta **58**, 525–538 (2019).

de Gans, B.-J., Kazancioglu, E., Meyer, W., and Schubert, U. S., “Ink-jet printing polymers and polymer libraries using micropipettes,” Macromol. Rapid Commun. **25**, 292–296 (2004).

Dinic, J., Zhang, Y., Jimenez, L. N., and Sharma. V., “Extensional relaxation times of dilute, aqueous polymer solutions,” ACS Macro Lett. **4**, 804–808 (2015).

Dong, H., Carr, W. W., and Morris J. F., “An experimental study of drop-on-demand drop formation,” Phys. Fluids **18**, 072102 (2006).

Gao, P., Hunter, A., Benavides, S., Summe, M. J., Gao, F., and Phillip, W. A., “Template synthesis of nanostructured polymeric membranes by inkjet printing,” ACS Appl. Mater. Interface **8**, 3386–3395 (2016).

Hirakata, S., Ishiyama, T., and Morita, N., “Printing stabilization resulting from the ink circulation path installed inside the print head and the jetting phenomenon during nozzle drying,” J. Imaging Sci. Techn. **58**, 050503 (2014).

Hoath, S. D., Harlen, O. G., and Hutchings, I. M., “Jetting behavior of polymer solutions in drop-on-demand inkjet printing,” J. Rheol. **56**, 1109–1127 (2012).

Hoath, S. D., Hsiao, W.-K., Jung, S., Martin, G. D., and Hutchings, I. M., “Drop speeds from drop-on-demand ink-jet print heads,” J. Imaging Sci. Techn. **57**, 010503 (2013a).

Hoath, S. D., Jung, S., and Hutchings, I. M., “A simple criterion for filament break-up in drop-on-demand inkjet printing,” Phys. Fluids **25**, 021701 (2013b).

Johnston, M. T. and Ewoldt, R. H., “Precision rheometry: Surface tension effects on low-torque measurements in rotational rheometers,” J. Rheol. **57**, 1515–1532 (2013).

Jovic, M., Hidalgo-Acosta, J. C., Lesch, A., Bassetto, V. C., Smirnov, E., Cortes-Salazar, F., and Girault, H. H., “Large-scale layer-by-layer inkjet printing of flexible iridium-oxide based pH sensors,” J. Electroanal. Chem. **819**, 384–390 (2018).

Kang, H., Lee, J. W., and Nam, Y., “Inkjet-printed multiwavelength thermoplasmonic images for anticounterfeiting applications,” ACS Appl. Mater. Interface **10**, 6764–6771 (2018).

Koivunen, R., Jutila, E., Bollström, R., and Gane, P., “Inkjet printed polyelectrolyte patterns for analyte separation on inherently porous microfluidic analytical designs,” Colloid Surf. A **522**, 218–232 (2017).

Koivunen, R., Jutila, E., Bollström, R., and Gane, P., “Investigating chromatographic interactions in porous pigment coatings between inkjettable polyelectrolytes and model colorant solutions,” Colloid Surf. A **579**, 123676 (2019).

Kwon, K.-S., Choi, Y.-S., and Go, J.-K., “Inkjet jet failures and their detection using piezo self-sensing,” Sens. Actuators A **201**, 335–341 (2013).

Laun, M., Auhl, D., Brummer, R., Dijkstra, D. J., Gabriel, C., Mangnus, M. A., Rüllmann, M., Zoetelief, W., and Handge, U. A., “Guidelines for checking performance and verifying accuracy of rotational rheometers: Viscosity measurements in steady and oscillatory shear (IUPAC Technical Report),” Pure Appl. Chem. **86**, 1945–1968 (2014).

Leigh, S. J., Bowen, J., and Preece, J. A., “Multiscale patterning of nanocomposite polyelectrolyte/nanoparticle films using inkjet printing and AFM scratching,” Mater. Res. Express **2**, 065301 (2015).

Li, Y., Dahhan, O., Filipe, C. D. M., Brennan, J. D., and Pelton, R. H., “Optimizing piezoelectric inkjet printing of silica sols for biosensor production,” J. Sol-Gel Sci. Techn. **87**, 657–664 (2018).

Limem, S. and Calvert, P., “Diffusion properties of inkjet printed ionic self-assembling polyelectrolyte hydrogels,” J. Mater. Chem. B **3**, 4569–4576 (2015).

Marquardt, W. and Nijman, J., “Experimental errors when using rotational rheometers,” Appl. Rheol. **3**, 120–129 (1993).

Muller, S. J., “Elastically-influenced instabilities in Taylor-Couette and other flows with curved streamlines: A review,” Korea-Aust. Rheol. J. **20**, 117–125 (2008).

Seo, M., Tsukamoto, T., and Norikane, Y., “A study on drying process of ink at the inkjet nozzle using a laser Doppler vibrometer,” in *2011 International Conference on Digital Printing Technologies* (Society for Imaging Science and Technology, 2011), pp. 347–350.

Stadler, F. J., “What are typical sources of error in rotational rheometry of polymer melts?,” Korea-Aust. Rheol. J. **26**, 277–291 (2014).

Tam, S. K., Fung, K. Y., Poon, G. S. H., and Ng, K. M., “Product design: Metal nanoparticle-based conductive inkjet inks,” AIChE J. **62**, 2740–2753 (2016).

Taylor, G. I., “Stability of a viscous liquid contained between two rotating cylinders,” Philos. Trans. R. Soc. A **223**, 289–343 (1923).

Turian, R. M., “Perturbation solution of the steady Newtonian flow in the cone and plate and parallel plate systems,” Ind. Eng. Chem. Fund. **11**, 361–368 (1972).

Vadillo, D. C., Tuladhar, T. R., Mulji, A. C., Jung, S., Hoath, S. D., and Mackley, M. R., “Evaluation of the inkjet fluid’s performance using the “Cambridge Trimaster” filament stretch and break-up device,” J. Rheol. **54**, 261–282 (2010a).

Vadillo, D. C., Tuladhar, T. R., Mulji, A. C., and Mackley, M. R., “The rheological characterization of linear viscoelasticity for ink jet fluids using piezo axial vibrator and torsion resonator rheometers,” J. Rheol. **54**, 781–795 (2010b).

Vasquez, G., Alvarez, E., and Navaza, J. M., “Surface tension of alcohol + water from 20 to 50 °C,” J. Chem. Eng. Data **40**, 611–614 (1995).

Velankar, S. S. and Giles, D., “How do I know if my phase angles are correct?,” Rheol. Bull. **76**, 8–20 (2007).

White, F., *Fluid Mechanics*, 4th ed. (McGraw-Hill, Singapore, 1999).

Wijshoff, H., “The dynamics of the piezo inkjet printhead operation,” Phys. Rep. **491**, 77–177 (2010).

Wolff, F. and Münstedt, H., “Artefacts of the storage modulus due to bubbles in polymeric fluids,” Rheol. Acta **52**, 287–289 (2013).

Wong, L.-Y., Lim, G.-H., Ye, T., Silva, F. B. S., Zhuo, J.-M., Png, R.-Q., Chua, S.-J., and Ho, P. K. H., “Jettable fluid space and jetting characteristics of a microprint head,” J. Fluid Mech. **713**, 109–122 (2012).

Zhang, Y., Huang, M., Kan, Y., Liu, L., Dai, X., Zheng, G., and Zhang, Z., “Influencing factors of viscosity measurement by rotational method,” Polym. Test. **70**, 144–150 (2018).